

**Supplemental Information**  
**Method to estimate thermal transients in reactors and determine their parameter sensitivity without a forward simulation**

SA Holdampf<sup>1</sup>, AG Osborne<sup>1,2</sup>, MR Deinert<sup>1,2,3</sup>

<sup>1</sup>Department of Mechanical Engineering

<sup>2</sup>Nuclear Science and Engineering

<sup>3</sup>Payne Institute for Public Policy

The Colorado School of Mines

**Supplementary Note S1. Governing Equations and Numerical Differencing Scheme for the Crank-Nicolson Finite Difference Thermal Response Model.** Here an overview of the finite difference numerical simulation is provided [1]. See Note 2 for detailed equations from the Jacobian sensitivity analysis.

**Methods.** Heat transfer within the nuclear fuel pin and surrounding coolant is governed by the transient, radial, one-dimensional heat equation with heat generation combined with Newton's law of cooling and an open system energy conservation equation, Eqs. S1-S3:

$$\rho c_p \frac{\partial T}{\partial t} = \frac{1}{r} \frac{\partial}{\partial r} \left( kr \frac{\partial T}{\partial r} \right) + \dot{q}_{gen}''' \quad (S1)$$

$$\frac{\partial q}{\partial t} = -hA(T(t) - T_b) \quad (S2)$$

$$\frac{\partial E}{\partial t} = \dot{m}(h_{in} - h_{out}) + \dot{q} \quad (S3)$$

In Eq. S1,  $\rho$  is density (kg/m<sup>3</sup>),  $c_p$  is specific heat capacity (J/kg-K),  $t$  is time (s),  $k$  is thermal conductivity (W/m-K),  $T$  is temperature (K), and  $\dot{q}_{gen}'''$  is volumetric heat generation (W/m<sup>3</sup>). Due to the radial temperature gradient being much higher than the axial gradient, only radial heat conduction is assumed [2]. Eq. S2 provides the convective boundary condition at the cladding-coolant border where  $q$  is the cladding-coolant heat transfer (J),  $h$  is the cladding-coolant heat transfer coefficient (W/m<sup>2</sup>-K),  $A$  is the cladding outer surface area (m<sup>2</sup>), and  $T_b$  is the coolant temperature (K). Eq. S3 provides an energy balance on an axial section of coolant.  $E$  is the energy stored in the coolant (J),  $\dot{m}$  is the coolant mass flow rate (kg/s),  $h_{in}$ ,  $h_{out}$  are specific enthalpies (J/kg), and  $\dot{q}$  is the heat transfer between the coolant and any surrounding surfaces (W).

Equation S1 is used within the void, fuel, and cladding. The fuel-cladding gap also uses Eq. S1 unless the user provides a heat transfer correlation for the gap. Heat generation is assumed to only occur in the fuel.

Equation S4 gives the energy balance used at boundaries between two materials [3].  $U$  is the internal energy (J),  $\dot{q}_{RHS}$  and  $\dot{q}_{LHS}$  represent heat transfer into the element from each direction (W), and  $\dot{q}_s$  is the source or sink term (W).

$$\frac{dU}{dt} = \rho c_p V \frac{\partial T}{\partial t} = \dot{q}_{RHS} + \dot{q}_{LHS} + \dot{q}_s \quad (S4)$$

An adiabatic boundary condition is used at the outer edge of the coolant unless a surrounding structure is present. If a structure is present, the adiabatic condition is applied at the outer surface of the structure. A fixed inlet coolant temperature provides the axial boundary condition. Equation S2 is the boundary condition at the cladding surface with it being substituted in for  $\dot{q}_{RHS}$  in Eq. S4 to generate the governing equation. A similar condition would be used if a surrounding structure exists for the boundary between coolant and structure. The coolant temperature is assumed to remain uniform in the radial direction. Equation S3 governs the axially discretized segments of the coolant channel.

A simple finite-difference approach in space and a Crank-Nicolson discretization scheme in time is used to discretize Eqs. S1, S3 and S4. Axial coolant nodes are offset by  $\Delta z/2$ , half of an axial discretization height, relative to the axial position of the radial nodes. This allows the coolant channel to be discretized as a series of open systems.

Thermophysical properties and convective heat transfer correlations are obtained from literature [2,4–6]. Three options are allowed for modelling heat transfer across the gap: solely conduction, a heat transfer correlation, or user-specified gap conductances. Properties vary in space and time and are updated based on each new temperature profile. Initial temperatures and properties can be obtained using a thermal resistor model or an initial profile input by the user. When the thermal resistor model is used, guesses at the average temperatures in each material are used to determine the material properties and iterated upon until the change in average temperature of the fuel is less than 0.001%. The temperature profile output after convergence provides the normal operating condition temperatures for use as the initial conditions in models simulating LOFA and overpower events as well as for calculating material properties in the transient model.

When obtaining the initial temperature profiles using a thermal resistor model, the coolant temperatures at the top of each axial segment can be calculated by using Eq. S5 and solving for  $T_{cool,i}$ .

$$\dot{m}c_{p,cool}(T_{cool,i} - T_{cool,i-1}) = \dot{q} \quad (S5)$$

$\dot{m}$  is the mass flow rate (kg/s).  $c_{p,cool}$  is the specific heat of the coolant (J/kg-K).  $T_{cool,i}$  is the coolant temperature at axial position  $i$  (K).  $\dot{q}$  is the total heat generation rate in the axial segment (W). Next a balance between the convective losses from the cladding outer surface and the heat generated in that axial segment of the pin can be used to determine the cladding surface temperature, Eq. S6.

$$2\pi r_{pin}\Delta z \left[ T_{clad,out} - \frac{(T_{cool,i} + T_{cool,i-1})}{2} \right] = \dot{q} \quad (S6)$$

$r_{pin}$  is the radius of the pin (m).  $\Delta z$  is the height of each axial discretization (m).  $T_{clad,out}$  is the outer surface temperature of the cladding (K). Thermal resistances can then be used to determine the temperatures throughout the rest of the cladding and additionally the gap if only conduction is considered, Eq. S7.

$$\frac{T_2 - T_1}{\dot{q}} = R = \frac{\ln\left(\frac{r_2}{r_1}\right)}{2\pi k_a \Delta z} \quad (S7)$$

$T_2$  is the temperature (K) at position  $r_2$  (m), and  $T_1$  is the temperature (K) at position  $r_1$  (m).  $k_a$  is the thermal conductivity (W/m-K) of material  $a$ , which separates the two nodes.  $R$  is the resistance across the thickness of gap or cladding (K/W). Equation S7 can also be used to determine the fuel surface temperature if only conduction is considered within the gap. However, if a gap conductance model is used, Eq. S2 is used for the heat transfer across the gap.

The steady-state, 1-D conduction equation with heat generation can be used to show that the temperatures in cylindrical and annular fuel are given by Eqs. S8 and S9 respectively.

$$T_f(r) = \dot{q} \frac{(r_f^2 - r^2)}{4\pi k_f r_f^2 \Delta z} + T_{f,out} \quad (S8)$$

$$T_f(r) = \dot{q} \frac{(r_f^2 - r^2)}{4\pi k_f (r_f^2 - r_v^2) \Delta z} + \dot{q} \frac{r_v^2}{2\pi k_f (r_f^2 - r_v^2) \Delta z} [\ln(r) - \ln(r_f)] + T_{f,out} \quad (S9)$$

Here  $r_f$  and  $r_v$  are the radii of the fuel and the void, respectively (m).  $k_f$  is the thermal conductivity of the fuel (W/m-K).  $T_{f,out}$  is the temperature at the outer surface of the fuel (K). At steady-state if a void is present, since all heat is moving into the coolant, the temperature of the void will equal that of the innermost fuel node for each axial segment. Similarly, if a structure is present, the temperature will match that within the coolant.

After the initial temperature profile is specified, equations S1, S3, and S4 are discretized using a finite difference scheme in space and the Crank-Nicolson method in time. Equations S10 and S11 provide the discretizations of Eqs. S1 and S3, respectively. Equation S10 is applied to nodes interior to the fuel and cladding domains as well as the gap domain if explicit gap conduction is selected. Equation S11 is derived from axially discretizing the coolant domain.  $i$  indicates the nodes' axial positions, and  $j$  provides the radial positions.

$$\rho c_p \left( \frac{T_{i,j}^{n+1} - T_{i,j}^n}{\Delta t} \right) = \frac{k}{r_j} \frac{T_{i,j+1}^{n+1} - T_{i,j-1}^{n+1}}{4\Delta r} + \frac{k}{r_j} \frac{T_{i,j+1}^n - T_{i,j-1}^n}{4\Delta r} + k \frac{T_{i,j+1}^{n+1} - 2T_{i,j}^{n+1} + T_{i,j-1}^{n+1}}{2\Delta r^2} + k \frac{T_{i,j+1}^n - 2T_{i,j}^n + T_{i,j-1}^n}{2\Delta r^2} + \dot{q}_s''', \quad (\text{S10})$$

$$\begin{aligned} \frac{V_j \rho_{cool} c_{p,cool} (T_{i,j}^{n+1} - T_{i,j}^n)}{2\Delta t} + \frac{V_{cool} \rho_{cool} c_{p,cool} (T_{i-1,j}^{n+1} - T_{i-1,j}^n)}{2\Delta t} + \frac{\dot{m} c_p}{2} (T_{i,j}^{n+1} - T_{i-1,j}^{n+1}) + \frac{\dot{m} c_p}{2} (T_{i,j}^n - T_{i-1,j}^n) \\ = A_{s,j-1} h \left( \frac{T_{i,j-1}^{n+1}}{2} - \frac{(T_{i,j}^{n+1} + T_{i-1,j}^{n+1})}{4} + \frac{T_{i,j-1}^n}{2} - \frac{(T_{i,j}^n + T_{i-1,j}^n)}{4} \right). \end{aligned} \quad (\text{S11})$$

When the energy balance, Eq. S4, is applied to the interfaces between the void and fuel, fuel and gap, or gap and cladding in the fuel pin,  $\dot{q}_{RHS}$  and  $\dot{q}_{LHS}$  can be expanded in terms of conductive heat transfer relations and discretized using Crank-Nicolson as shown in Eq. S12. When heat transfer correlations or user-defined conductances are used to model the gap, the Crank-Nicolson discretization of Eq. S4 for the fuel-gap and gap-cladding interfaces are shown in Eqs. S13 and S14. When applied to the interface between the cladding and the coolant,  $\dot{q}_{RHS}$  in Eq. S4 can be expanded in terms of convective heat transfer relations, Eq. S2, and discretized as shown in Eq. S15.

$$\begin{aligned} \frac{V_a \rho_a c_{p,a} (T_{i,j}^{n+1} - T_{i,j}^n)}{\Delta t} + \frac{V_b \rho_b c_{p,b} (T_{i,j}^{n+1} - T_{i,j}^n)}{\Delta t} = \frac{A_{s,j-1/2} k_a (T_{i,j-1}^{n+1} - T_{i,j}^{n+1})}{2\Delta r_a} + \frac{A_{s,j-1/2} k_a (T_{i,j-1}^n - T_{i,j}^n)}{2\Delta r_a} \\ + \frac{A_{s,j+1/2} k_b (T_{i,j+1}^{n+1} - T_{i,j}^{n+1})}{2\Delta r_b} + \frac{A_{s,j+1/2} k_b (T_{i,j+1}^n - T_{i,j}^n)}{2\Delta r_b} + \dot{q}_s \end{aligned} \quad (\text{S12})$$

$$\begin{aligned} \frac{V_j \rho_f c_{p,f} (T_{i,j}^{n+1} - T_{i,j}^n)}{\Delta t} = \frac{A_{s,j-1/2} k_f (T_{i,j-1}^{n+1} - T_{i,j}^{n+1})}{2\Delta r_f} + \frac{A_{s,j-1/2} k_f (T_{i,j-1}^n - T_{i,j}^n)}{2\Delta r_f} \\ + h_{g,i} A_{s,j} \left( \frac{(T_{i,j+1}^{n+1} - T_{i,j}^{n+1})}{2} + \frac{(T_{i,j+1}^n - T_{i,j}^n)}{2} \right) + \dot{q}_s \end{aligned} \quad (\text{S13})$$

$$\begin{aligned} \frac{V_j \rho_{cl} c_{p,cl} (T_{i,j}^{n+1} - T_{i,j}^n)}{\Delta t} \\ = \frac{A_{s,j+1/2} k_{cl} (T_{i,j+1}^{n+1} - T_{i,j}^{n+1})}{2\Delta r_{cl}} + \frac{A_{s,j+1/2} k_{cl} (T_{i,j+1}^n - T_{i,j}^n)}{2\Delta r_{cl}} \\ + h_{g,i} A_{s,j-1} \left( \frac{(T_{i,j-1}^{n+1} - T_{i,j}^{n+1})}{2} + \frac{(T_{i,j-1}^n - T_{i,j}^n)}{2} \right) \end{aligned} \quad (\text{S14})$$

$$\frac{V_j \rho_{cl} c_{p,cl} (T_{i,j}^{n+1} - T_{i,j}^n)}{\Delta t} = \frac{A_{s,j-1/2} k_{cl} (T_{i,j-1}^{n+1} - T_{i,j}^{n+1})}{2\Delta r_{cl}} + \frac{A_{s,j-1/2} k_{cl} (T_{i,j-1}^n - T_{i,j}^n)}{2\Delta r_{cl}} \quad (\text{S15})$$

$$+A_{s,j}h\left(\frac{(T_i^{n+1} + T_{i-1}^{n+1})}{4} - \frac{T_{i,j}^{n+1}}{2} + \frac{(T_i^n + T_{i-1}^n)}{4} - \frac{T_{i,j}^n}{2}\right)$$

Here,  $i$  and  $j$  are the axial and radial spatial position indices,  $V_a$  is the volume of an element in material  $a$  ( $\text{m}^3$ ),  $A_s$  is the inner or outer surface area of the element ( $\text{m}^2$ ),  $\Delta t$  is the time step (s),  $\Delta r_a$  is the size of radial discretizations in material  $a$  (m),  $\dot{m}$  is the coolant mass flow rate (kg/s), and  $h_{g,i}$  is the gap conductance ( $\text{W}/\text{m}^2\text{-K}$ ). Heat transfer between the surface of the cladding and the coolant is computed using the average coolant temperature between two vertical coolant nodes. To obtain the temperatures of the first node in the coolant and the neighboring cladding node,  $T_{i-1}^{n+1}$  is set equal to the inlet temperature of the bulk coolant in Eqs. S11 and S15 when  $i = 1$ .

Once discretized the coupled equations can be written in matrix form, Eq. S16:

$$AT = f \quad (\text{S16})$$

Coefficients of unknown future temperatures are collected in matrix,  $A$ , and the vector,  $f$  represents known previous time step quantities. Equation S5 was solved at each timestep using the backslash operator from the standard Matlab matrix solver library [7].

The validation results in Figures S2 and S3 based on comparison to the CABRI BI1 experiment were originally published in [1]. Here those results and other validation results are presented to provide confidence in the numerical simulation used as a baseline comparison for the Jacobian based model.

Figure S1 provides the relative power profile used when modeling the CABRI BI1 experiment fuel pin. The SAS-SFR and experimental curves were obtained from [8] and extracted using ImageJ's plugin Figure Calibration [9,10]. The peak linear power used in the model was calculated to be 63.4 kW/m after interpolating the SAS-SFR curve, which has a peak linear power of 62.11 kW/m, and normalizing to ensure the total power is 35,738 kW. The linear power used in modelling each axial segment of the pin is the value at the axial center position of the segment.

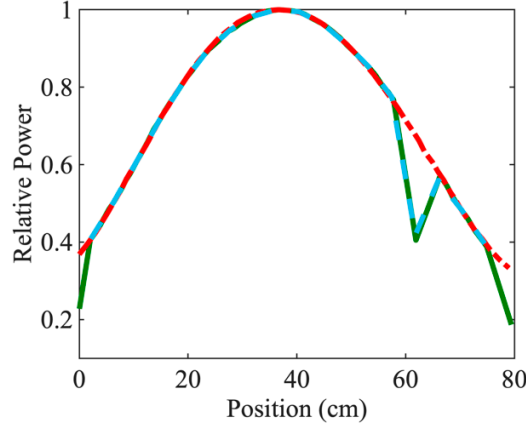


**Figure S1.** Relative power profile used in modeling the CABRI BI1 experiment. Experimental power profile shown by red dash-dot line, SAS-SFR profile by the solid green curve [8]. The curve used by our model is shown by the dashed blue curve.

In the CABRI BI1 test loop, a niobium structure surrounding the pin and coolant isolates the test channel from the rest of the reactor. The dimension of the niobium structure from the CABRI experiment is confidential and cannot be provided here. Those interested in greater details on the CABRI experiment should reach out to IRSN Centre de Cadarache [11]. Our code can account for this type of setup through a user-enabled switch and user specification of the geometry, thermophysical properties and mesh parameters of the isolating structure.

Equation S3 in the main paper can be used to model the heat losses from the coolant to the isolating structure through inclusion of an additional term  $\dot{q}_{iso}$  on its right-hand side, Eq. S17:

$$\dot{q}_{iso} = A_{s,j+1} h_s \left( \frac{T_{l,j+1}^{n+1}}{2} - \frac{(T_{l,j}^{n+1} + T_{l-1,j}^{n+1})}{4} + \frac{T_{l,j+1}^n}{2} - \frac{(T_{l,j}^n + T_{l-1,j}^n)}{4} \right) \quad (\text{S17})$$

Equation S15 can be used to represent heat transfer at the nodes at the edge of the structure with a slight modification.  $j - 1/2$  indices must be changed to  $j + 1/2$  indices since the structure is on the opposite side of the coolant. Equation S10 can be applied for all interior nodes in the structure as with the interior of the fuel and cladding.

**Fuel Parameters.** Experimental results from the CABRI BI1 experiment and the SAS-SFR model of the experiment were used to validate our model. The basis for the CABRI BI1 experiment was a MOX pin with a burnup of  $\leq 1$  a/o. The pin was placed into a sodium test loop in the center of the CABRI pool-type research reactor. The power and coolant flow in the core were configured to replicate normal and accident conditions while the

test loop isolated the experimental pin thermally from the remainder of the core. The BI1 experiment was a loss of flow transient that continued until the sodium boiled [8].

SAS-SFR, the Safety Analysis System-Sodium Fast Reactor code is based on SAS4A developed by Argonne National Laboratory and has been created through the collaboration of KIT/INR, CEA, IRSN, and Japan Atomic Energy Agency. SAS-SFR and SAS4A model subassemblies as single representative pins and uses the transient heat conduction equation coupled with an energy equation and point kinetics equations. The governing equations are discretized using a finite difference method [12,13]. Both codes can account for fuel deformation and clad melting [8,13–15].

The geometry of the test pin from the CABRI BI1 experiment used in the validation of the model is shown in Table S1. Due to the 1 at.% burnup, we assume the O/M ratio increases to 2.0. The porosity used is half the fabricated porosity or 3.1%.

**Table S1.** Design parameters for the CABRI MOX pin [8].

<b>Core</b>	<b>Mixed Oxide</b>
Fuel Composition	0.8U0.2PuO <sub>2</sub>
Coolant	Sodium
Void Fill Fluid	Helium
Cladding	Steel
Inlet coolant temperature (K)	677.5
Initial coolant mass flow rate (kg/s)	0.1592
Fissile power (W)	35,738
Peak power axial location (cm)	36.18
Void radius (cm)	0.0475
Fuel pellet diameter (cm)	0.3333
Cladding thickness (cm)	0.0505
Pin diameter (cm)	0.7676

For modeling the CABRI experiment, fuel thermal conductivity comes from [16]. Fuel density and specific heat largely come from correlations in [17] with the specific heat requiring U and Pu dioxide equations from [4]. All cladding property correlations are obtained from [2]. Coolant density and specific heat equations are in [4]. For the coolant dynamic viscosity, the equation is found in [18]. The Nusselt number correlation for the pitch to diameter ratio is used to obtain the heat transfer coefficient between the cladding and coolant [2,5].

No gap width is specified as SAS-SFR uses URGAP for modeling the gap resistance under the assumption of a closed gap [19,20]. To account for the resistance in our model, gap conductance values at each axial position were back-computed using Figure 11 in [15] and Table 7 and Figure 3 in [8]. ImageJ and its Figure Calibration Plugin were used to pull data from the plots, including outer fuel temperatures, inner cladding temperatures, and the relative power profile [9,10]. The data were then substituted into Eq. S18, which governs the heat transfer across the gap at steady-state when a conductance model is used.

$$\dot{q} = A_f h_g (T_{f,out} - T_{cl,in}) \quad (S18)$$

$\dot{q}$  is the heat being transferred across the gap at steady-state (W).  $A_f$  is surface area of the fuel outer surface (m<sup>2</sup>).  $h_g$  is the gap conductance, or heat transfer coefficient (W/m<sup>2</sup>-K).  $T_{f,out}$  is the temperature of the outer surface of the fuel (K).  $T_{cl,in}$  is the temperature at the inner surface of the cladding (K). Equation S18 was rearranged and solved for the gap conductance.

During the CABRI BI1 transient, the reduction in mass flow rate is governed by Eq. S19:

$$\dot{m} = \frac{\dot{m}_0}{1 + \frac{t}{8}}, \quad (S19)$$

where  $\dot{m}$  is the time dependent mass flow rate (kg/s),  $\dot{m}_0$  is the initial mass flow rate (kg/s), and  $t$  is how much time has elapsed since the initiation of the loss of flow event (s). SAS-SFR and experimental results were drawn from [8] and [15] using ImageJ and the Figure Calibration Plugin [9,10].

**Validation Results.** After the thermal response model has been run to simulate the CABRI BI1 experiment, a coefficient of determination,  $R^2$ , is used to determine how well the experimental results fit to our model and the SAS-SFR model. Equation S20 is used to calculate  $R^2$ :

$$R^2 = 1 - \frac{SSE}{SSTO}. \quad (S20)$$

Here,  $SSE$  is the regression sum of squares, and  $SSTO$  is the total sum of squares.

The left panel of Fig. S2 shows the axial coolant temperature profile prior to the transient computed by our model, the SAS-SFR model, and experimental thermocouple measurements.



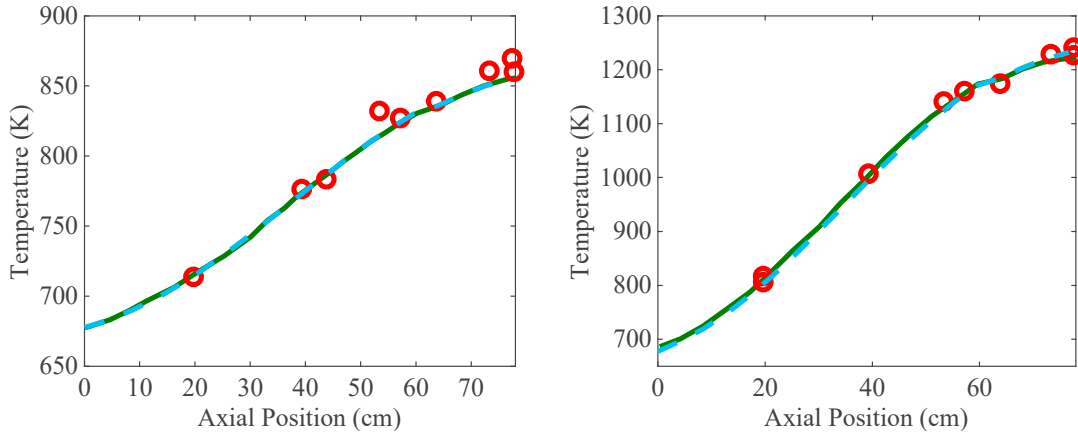


**Figure S2. Axial coolant temperature profiles.** (left) Axial coolant temperature at steady state prior to the loss of flow event. (right) Axial coolant temperature at  $t=20$  s after the loss of flow event begins. Experimental results shown by red circles, SAS-SFR model results by the solid green curve. The results computed by our model are shown by the dashed blue curve.

The coefficient of determination,  $R^2$ , for the fit of the experimental results to our model is 0.9699 and to the SAS-SFR results is 0.9693. The axial coolant profile 20 seconds into the transient is shown in the right panel of Fig. S2. After 20 seconds, the coolant begins to boil, however, two-phase heat transfer is not currently supported by our model. The  $R^2$  value for the fit of the experimental results to our model is 0.9954 and to the SAS-SFR results is 0.9975. The temperature of the coolant as a function of time was also computed at axial locations 20, 39, 63 and 77 cm above the bottom end of the fuel, Fig. S3. The  $R^2$  value for the fit of the experimental results to our model at 20 cm is 0.9924 and to the SAS-SFR result is 0.9573. The coefficient of determination for the fit to the current model at 39 cm is 0.9402 and to the SAS-SFR results at 39 cm is 0.9776. The  $R^2$  values at 63 cm is 0.9980 for the current results and 0.9985 for the SAS-SFR results and for the fit to our current model and SAS-SFR model at 77 cm are 0.9969 and 0.9964, respectively.

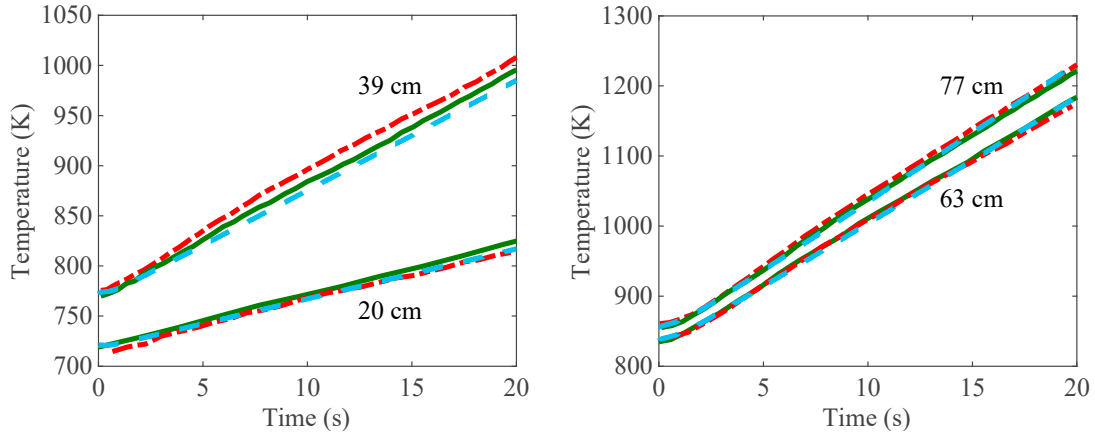


**Figure S3. Coolant temperatures during the CABRI loss of flow event. (left)** results for 20 cm and 39 cm elevation. **(right)** Results for 63 cm and 77 cm elevation. Experimental results shown by red dash-dot line, SAS-SFR model results by the solid green curve. The results computed by our model are shown by the dashed blue curve.

As experimental fuel and cladding temperature measurements are not available, our model is compared to the results of the SAS-SFR simulation provided in [8,15]. The axial inner fuel temperature profile prior to the start of the transient is shown in Fig. S4. The coefficient of determination,  $R^2$  between our model and the SAS-SFR model is 0.9902.

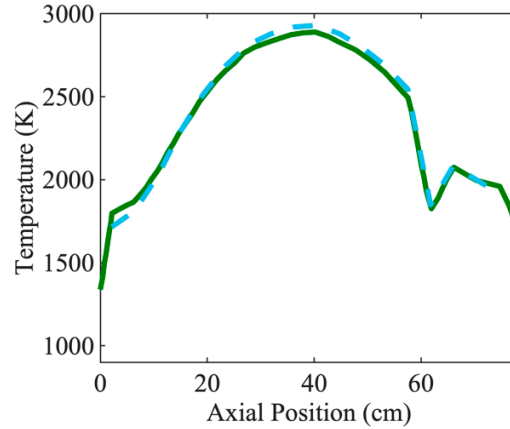


**Figure S4.** Inner fuel temperature prior to the loss of flow event. The SAS-SFR profile is shown by the solid green curve. The curve used by our model is shown by the dashed blue curve.

The axial outer fuel temperature profile prior to the start of the transient is shown in Fig. S5. The coefficient of determination,  $R^2$ , between our model and the SAS-SFR model is 0.9992.

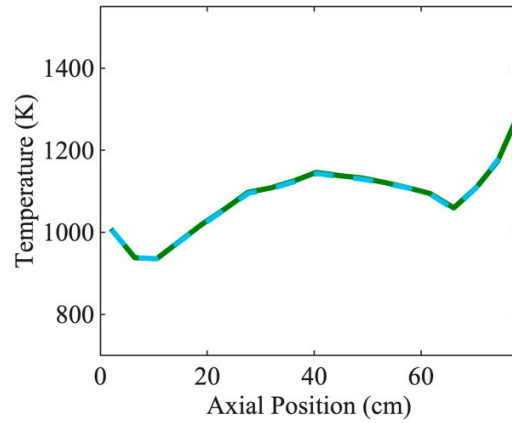


**Figure S5.** Outer fuel temperature prior to the loss of flow event. The SAS-SFR profile is shown by the solid green curve. The curve used by our model is shown by the dashed blue curve.

The axial average fuel temperature profile prior to the start of the transient is shown in Fig. S6. The averaging is performed by weighting the fuel temperatures by the volume of each element. The coefficient of determination,  $R^2$ , between our model and the SAS-SFR model is 0.9983.

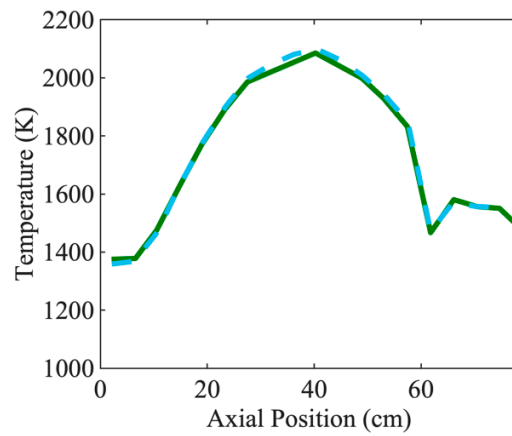


**Figure S6.** Average fuel temperature prior to the loss of flow event. The SAS-SFR profile is shown by the solid green curve. The curve used by our model is shown by the dashed blue curve.

The axial inner cladding temperature profile prior to the start of the transient is shown in Fig. S7. The coefficient of determination,  $R^2$ , for the fit of our model to the SAS-SFR model is 0.9988.

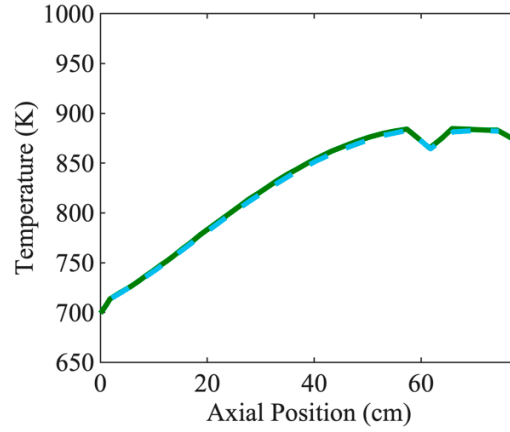


**Figure S7.** Inner cladding temperature prior to the loss of flow event. The SAS-SFR profile is shown by the solid green curve. The curve used by our model is shown by the dashed blue curve.

The axial outer cladding temperature profile prior to the start of the transient is shown in Fig. S8. The coefficient of determination,  $R^2$ , for the fit of our model to the SAS-SFR model is 0.9987.

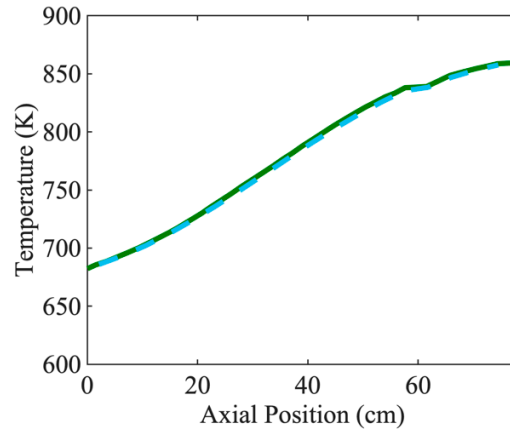


**Figure S8.** Outer cladding temperature prior to the loss of flow event. The SAS-SFR profile is shown by the solid green curve. The curve used by our model is shown by the dashed blue curve.

**Convergence Testing.** The model was run through convergence tests with respect to radial and temporal discretizations. An axial convergence test was not performed since the number of axial discretizations used in the SAS-SFR model of the CABRI BI1 model is known [8] and kept constant for all other simulations. The relative difference in a given result after a mesh reduction,  $\epsilon$ , is given by Eq. S21:

$$\epsilon = \left| \frac{T_1 - T_0}{T_0} \right|, \quad (\text{S21})$$

where  $T_0$  is the result at the selected level of discretization (K), and  $T_1$  is the result at the finer level of discretization (K). The mesh was made finer until  $\epsilon$  reduced to order  $10^{-4}$  for the radial and temporal cases with meshes becomes two times finer in the radial case and ten times finer in the temporal case.  $\Delta r_v$ ,  $\Delta r_f$ , and  $\Delta r_{cl}$  are radial element sizes in the void, fuel, cladding, and isolating structure respectively (mm). Final mesh sizes of  $\Delta r_v \leq 5.28 \times 10^{-2}$  mm,  $\Delta r_f \leq 3.18 \times 10^{-2}$  mm,  $\Delta r_{cl} \leq 2.66 \times 10^{-2}$  mm, and  $\Delta t \leq 0.01$ s were found to result in changes less than  $10^{-4}$ . The surrounding surface discretization size is not provided due to the coolant and structure dimensions being confidential. The number of nodes within the void, fuel, and cladding associated with these radial element sizes are  $N_v=10$ ,  $N_f=100$ , which includes void and fuel nodes, and  $N_d=20$ . Both CABRI BI1 and BN-800 models in this work use the same spatial node parameters. This corresponds to radii values of  $\Delta r_f = 2.92 \times 10^{-2}$  mm and  $\Delta r_{cl} = 2.11 \times 10^{-2}$  mm as the BN800 model does not include a void. The temporal mesh size  $\Delta t$  is decreased to 0.0001s in the analysis of the BN-800 temperature response to better model the instantaneously applied perturbations presented in the main text.

The CABRI BI1 model was compared to a steady-state solution obtained by evaluating a one-dimensional thermal resistor model. Here, the initial temperature of the entire pin was set to the temperature of the coolant inlet and the simulation ran until the system reached steady-state. The properties were held constant throughout this simulation. This crosscheck ensured that the transient model would predict the same asymptotic temperatures as the thermal resistor model. The temperature profiles from both cases were subtracted and normalized by the steady-state temperatures to determine how well they agree. Figure S9 gives the maximum relative difference between the two models as a function of time at the centerline and at the outer surface of the cladding.

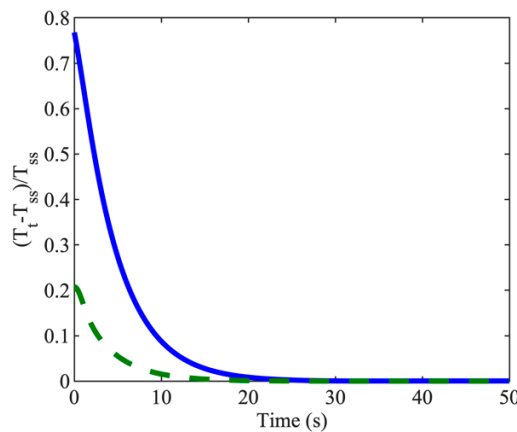


**Figure S9.** Maximum Relative Differences between the Steady-State Thermal Resistor and Transient Finite Difference Models at the Centerline (Blue Line) and Outer Cladding (Green Dashed Line)

After 37.96 seconds, the models agree to  $9.97 \times 10^{-4}$  at the pin centerline with better agreement at the outer cladding further validating the Crank-Nicolson finite difference code. A check of conservation of energy was performed where the change in energy of the coolant was compared to the heat generated within the fuel, these agreed within  $8.87 \times 10^{-4}$ . The check for convergence to steady state was repeated with the BN-800 geometry with MOX fuel and a time step of 0.001 s. The relative difference fell below  $10^{-4}$  after 18.76 seconds with a relative difference in heat generation compared to removal via the coolant of  $5.37 \times 10^{-4}$  at that time.

**Lumped Capacitance Crosscheck.** A comparison to an analytical lumped capacitance model was performed. The geometry of the BN-800 was modeled with mixed oxide fuel for this comparison. First, an analytical lumped capacitance equation was formulated, which represents the limit of the thermal conductivities and coolant specific heat capacity going to infinity [3]. The governing lumped capacitance equation and its solution can be written as Eqs. (S22) and (S23).

$$(\rho_v c_{p,v} V_v + \rho_f c_{p,f} V_f + \rho_g c_{p,g} V_g + \rho_c c_{p,c} V_c) \frac{dT}{dt} = \dot{q}_{gen} - h A_s (T - T_{cool}) \quad (S22)$$

$$T_{lc}(t) = T_{cool} + (T_i - T_{cool}) e^{\frac{-A_s h t}{\rho_v c_{p,v} V_v + \rho_f c_{p,f} V_f + \rho_g c_{p,g} V_g + \rho_c c_{p,c} V_c}} - \left( \frac{\dot{q}_{gen}}{A_s h} \right) e^{\frac{-A_s h t}{\rho_v c_{p,v} V_v + \rho_f c_{p,f} V_f + \rho_g c_{p,g} V_g + \rho_c c_{p,c} V_c}} + \frac{\dot{q}_{gen}}{A_s h} \quad (S23)$$

$\rho$  is the density (kg/m<sup>3</sup>).  $c_p$  is the specific heat (J/kg-K).  $V$  is the volume of a certain material (m<sup>3</sup>).  $t$  is time (s).  $\dot{q}_{gen}$  is the total heat generated in the axial segment (W).  $A_s$  is the outer surface area of an axial cladding segment (m<sup>2</sup>).  $T_{cool}$  is the temperature of the coolant since it is treated as an infinite heat sink (K), and  $T_i$  is the initial temperature of the fuel pin (K). If a gap conductance model is used, the gap term goes away.

The solution is applied at each axial position. In the lumped capacitance model, the coolant channel is treated as an infinite heat sink where the temperature remains the inlet temperature, 627.15 K. Here a temporal mesh size  $\Delta t = 0.0001$  s is used. The accuracy of the numerical model is tested by solving the lumped capacitance equation and then comparing it to the numerical finite difference outputs for high values of thermal conductivity and coolant specific heat. The maximum relative difference with respect to the lumped capacitance model stays below  $10^{-5}$  for the duration of the simulation providing confidence in the numerical model.

**Supplementary Note S2. Governing Equations and Numerical Differencing Scheme for the Jacobian Terms.** The equations used in the Jacobian come from discretizing explicit Euler finite difference forms of the heat equation and energy balances, Eq. S1, S3, and S4, as well as standard property equations [4,17,21,22]. Equation S24 provides the discretized form of Eq. S1 for interior fuel and cladding nodes that the Jacobian second partial derivatives are applied to.

$$\begin{aligned} \frac{\partial T_{i,j}}{\partial t} = & \frac{1}{\rho_{i,j}c_{i,j}} \left( \frac{k_{i,j+1} - k_{i,j-1}}{r_{j+1} - r_{j-1}} \right) \left( \frac{T_{i,j+1} - T_{i,j-1}}{r_{j+1} - r_{j-1}} \right) + \frac{k_{i,j}}{\rho_{i,j}c_{i,j}} \left( \frac{T_{i,j+1} - 2T_{i,j} + T_{i,j-1}}{(r_{j+1} - r_j)^2} \right) \\ & + \frac{k_{i,j}}{\rho_{i,j}c_{i,j}r_j} \left( \frac{T_{i,j+1} - T_{i,j-1}}{r_{j+1} - r_{j-1}} \right) + \frac{\dot{q}'''}{\rho_{i,j}c_{i,j}} \end{aligned} \quad (S24)$$

Equation S25 provides the discretized form of Eq. S4 for the boundary between the fuel and gap when a gap heat conductance is calculated. If the indices are rearranged with j+1 moving to j-1 and j-1 moving to j+1 and the arrangement of the radii terms flipped, the same equation with no generation can be used for the cladding-gap boundary equation. Equation S25 can also be used for the coolant-cladding boundary by removing the heat generation term and replacing  $T_{j+1}$  with an average of the two neighboring coolant nodes due to the coolant nodes having a half axial spacing offset.

$$\begin{aligned} \frac{\partial T_{i,j}}{\partial t} = & \frac{(k_{i,j-1} + k_{i,j}) \frac{(r_j + r_{j-1})}{2}}{\left( \rho_{i,j}c_{p,i,j} \left[ r_j^2 - \left( \frac{(r_j + r_{j-1})}{2} \right)^2 \right] \right) \Delta r} (T_{i,j-1} - T_{i,j}) + \frac{h2r_j}{\left( \rho_{i,j}c_{p,i,j} \left[ r_j^2 - \left( \frac{(r_j + r_{j-1})}{2} \right)^2 \right] \right)} (T_{j+1} - T_j) \\ & + \frac{\dot{q}'''}{(\rho_{i,j}c_{p,i,j})} \end{aligned} \quad (S25)$$

Equations S26 through S33 are given below and show how discretizations for each property are taken. These are the equations that are substituted into the Jacobian Eq. 1 for temperature derivatives.

$$\frac{\partial}{\partial T_{i,j}} \frac{\partial T_{i,j}}{\partial t} = \frac{k_{i,j}}{\rho_{i,j}c_{i,j}} \left( \frac{-2}{(r_{j+1} - r_j)^2} \right) \quad (S26)$$

$$\begin{aligned} \frac{\partial}{\partial T_{i,j+1}} \frac{\partial T_{i,j}}{\partial t} = & \frac{1}{\rho_{i,j}c_{i,j}} \left( \frac{k_{i,j+1} - k_{i,j-1}}{r_{j+1} - r_{j-1}} \right) \left( \frac{1}{r_{j+1} - r_{j-1}} \right) + \frac{k_{i,j}}{\rho_{i,j}c_{i,j}} \left( \frac{1}{(r_{j+1} - r_j)^2} \right) \\ & + \frac{k_{i,j}}{\rho_{i,j}c_{i,j}r_j} \left( \frac{1}{r_{j+1} - r_{j-1}} \right) \end{aligned} \quad (S27)$$

$$\begin{aligned} \frac{\partial}{\partial T_{i,j-1}} \frac{\partial T_{i,j}}{\partial t} &= \frac{1}{\rho_{i,j} c_{i,j}} \left( \frac{k_{i,j+1} - k_{i,j-1}}{r_{j+1} - r_{j-1}} \right) \left( \frac{-1}{r_{j+1} - r_{j-1}} \right) + \frac{k_{i,j}}{\rho_{i,j} c_{i,j}} \left( \frac{1}{(r_{j+1} - r_j)^2} \right) \\ &\quad + \frac{k_{i,j}}{\rho_{i,j} c_{i,j} r_j} \left( \frac{-1}{r_{j+1} - r_{j-1}} \right) \end{aligned} \quad (S28)$$

$$\frac{\partial}{\partial k_{i,j}} \frac{\partial T_{i,j}}{\partial t} = \frac{1}{\rho_{i,j} c_{i,j}} \left( \frac{T_{i,j+1} - 2T_{i,j} + T_{i,j-1}}{(r_{j+1} - r_j)^2} \right) + \frac{1}{\rho_{i,j} c_{i,j} r_j} \left( \frac{T_{i,j+1} - T_{i,j-1}}{r_{j+1} - r_{j-1}} \right) \quad (S29)$$

$$\frac{\partial}{\partial k_{i,j+1}} \frac{\partial T_{i,j}}{\partial t} = \frac{1}{\rho_{i,j} c_{i,j}} \left( \frac{1}{r_{j+1} - r_{j-1}} \right) \left( \frac{T_{i,j+1} - T_{i,j-1}}{r_{j+1} - r_{j-1}} \right) \quad (S30)$$

$$\frac{\partial}{\partial k_{i,j-1}} \frac{\partial T_{i,j}}{\partial t} = \frac{1}{\rho_{i,j} c_{i,j}} \left( \frac{-1}{r_{j+1} - r_{j-1}} \right) \left( \frac{T_{i,j+1} - T_{i,j-1}}{r_{j+1} - r_{j-1}} \right) \quad (S31)$$

$$\begin{aligned} \frac{\partial}{\partial \rho_{i,j}} \frac{\partial T_{i,j}}{\partial t} &= \frac{-1}{\rho_{i,j}^2 c_{i,j}} \left( \frac{k_{i,j+1} - k_{i,j-1}}{r_{j+1} - r_{j-1}} \right) \left( \frac{T_{i,j+1} - T_{i,j-1}}{r_{j+1} - r_{j-1}} \right) - \frac{k_{i,j}}{\rho_{i,j}^2 c_{i,j}} \left( \frac{T_{i,j+1} - 2T_{i,j} + T_{i,j-1}}{(r_{j+1} - r_j)^2} \right) \\ &\quad - \frac{k_{i,j}}{\rho_{i,j}^2 c_{i,j} r_j} \left( \frac{T_{i,j+1} - T_{i,j-1}}{r_{j+1} - r_{j-1}} \right) - \frac{\dot{q}'''}{\rho_{i,j}^2 c_{i,j}} \end{aligned} \quad (S32)$$

$$\begin{aligned} \frac{\partial}{\partial c_{i,j}} \frac{\partial T_{i,j}}{\partial t} &= -\frac{1}{\rho_{i,j} c_{i,j}^2} \left( \frac{k_{i,j+1} - k_{i,j-1}}{r_{j+1} - r_{j-1}} \right) \left( \frac{T_{i,j+1} - T_{i,j-1}}{r_{j+1} - r_{j-1}} \right) \\ &\quad - \frac{k_{i,j}}{\rho_{i,j} c_{i,j}^2} \left( \frac{T_{i,j+1} - 2T_{i,j} + T_{i,j-1}}{(r_{j+1} - r_j)^2} \right) - \frac{k_{i,j}}{\rho_{i,j} c_{i,j}^2 r_j} \left( \frac{T_{i,j+1} - T_{i,j-1}}{r_{j+1} - r_{j-1}} \right) - \frac{\dot{q}'''}{\rho_{i,j} c_{i,j}^2} \end{aligned} \quad (S33)$$

To demonstrate how the derivatives of a property correlation are obtained, Eq. S34 gives the equation for fuel thermal conductivity used in our BN800 MOX model [17]. Eq. S35 shows the temporal derivative of Eq. S34. Lastly, Eqs S36 through S43 give the second derivatives with respect to temperature, thermal conductivity, density, and specific heat at that node location.

$$k_{i,j} = \left( \frac{1}{0.037 + 2.37 \times 10^{-4} T_{i,j}} + 78.9 \times 10^{-12} T_{i,j}^3 \right) \quad (S34)$$

$$\frac{dk_{i,j}}{dt} = \left( \frac{-2.37 \times 10^{-4} \frac{\partial T_{i,j}}{\partial t}}{(0.037 + 2.37 \times 10^{-4} T_{i,j})^2} + 3 \times 78.9 \times 10^{-12} T_{i,j}^2 \frac{\partial T_{i,j}}{\partial t} \right) \quad (S35)$$



$$\frac{\partial}{\partial T_{i,j}} \frac{\partial k_{f,j}}{\partial t} = \left( \frac{-2.37 \times 10^{-4} \frac{\partial}{\partial T_{i,j}} \frac{\partial T_{i,j}}{\partial t}}{(0.037 + 2.37 \times 10^{-4} T_{i,j})^2} + \frac{2 \times 2.37 \times 10^{-4} \times 2.37 \times 10^{-4} \frac{\partial T_{i,j}}{\partial t}}{(0.037 + 2.37 \times 10^{-4} T_j)^3} \right. \\ \left. + 3 \times 78.9 \times 10^{-12} T_{i,j}^2 \frac{\partial}{\partial T_{i,j}} \frac{\partial T_{i,j}}{\partial t} + 2 \times 3 \times 78.9 \times 10^{-12} T_{i,j} \frac{\partial T_{i,j}}{\partial t} \right) \quad (S36)$$

$$\frac{\partial}{\partial T_{i,j+1}} \frac{\partial k_{i,j}}{\partial t} = \left( \frac{-2.37 \times 10^{-4} \frac{\partial}{\partial T_{i,j+1}} \frac{\partial T_{i,j}}{\partial t}}{(0.037 + 2.37 \times 10^{-4} T_{i,j})^2} + 3 \times 78.9 \times 10^{-12} T_{i,j}^2 \frac{\partial}{\partial T_{i,j+1}} \frac{\partial T_{i,j}}{\partial t} \right) \quad (S37)$$

$$\frac{\partial}{\partial T_{i,j-1}} \frac{\partial k_{i,j}}{\partial t} = \left( \frac{-2.37 \times 10^{-4} \frac{\partial}{\partial T_{i,j-1}} \frac{\partial T_{i,j}}{\partial t}}{(0.037 + 2.37 \times 10^{-4} T_{i,j})^2} + 3 \times 78.9 \times 10^{-12} T_{i,j}^2 \frac{\partial}{\partial T_{i,j-1}} \frac{\partial T_{i,j}}{\partial t} \right) \quad (S38)$$

$$\frac{\partial}{\partial k_{i,j}} \frac{\partial k_{i,j}}{\partial t} = \left( \frac{-2.37 \times 10^{-4} \frac{\partial}{\partial k_{i,j}} \frac{\partial T_{i,j}}{\partial t}}{(0.037 + 2.37 \times 10^{-4} T_{i,j})^2} + 3 \times 78.9 \times 10^{-12} T_{i,j}^2 \frac{\partial}{\partial k_{i,j}} \frac{\partial T_{i,j}}{\partial t} \right) \quad (S39)$$

$$\frac{\partial}{\partial k_{i,j+1}} \frac{\partial k_{i,j}}{\partial t} = \left( \frac{-2.37 \times 10^{-4} \frac{\partial}{\partial k_{i,j+1}} \frac{\partial T_{i,j}}{\partial t}}{(0.037 + 2.37 \times 10^{-4} T_{i,j})^2} + 3 \times 78.9 \times 10^{-12} T_{i,j}^2 \frac{\partial}{\partial k_{i,j+1}} \frac{\partial T_{i,j}}{\partial t} \right) \quad (S40)$$

$$\frac{\partial}{\partial k_{i,j-1}} \frac{\partial k_{i,j}}{\partial t} = \left( \frac{-2.37 \times 10^{-4} \frac{\partial}{\partial k_{i,j-1}} \frac{\partial T_{i,j}}{\partial t}}{(0.037 + 2.37 \times 10^{-4} T_{i,j})^2} + 3 \times 78.9 \times 10^{-12} T_{i,j}^2 \frac{\partial}{\partial k_{i,j-1}} \frac{\partial T_{i,j}}{\partial t} \right) \quad (S41)$$

$$\frac{\partial}{\partial \rho_{i,j}} \frac{\partial k_{i,j}}{\partial t} = \left( \frac{-2.37 \times 10^{-4} \frac{\partial}{\partial \rho_{i,j}} \frac{\partial T_{i,j}}{\partial t}}{(0.037 + 2.37 \times 10^{-4} T_{i,j})^2} + 3 \times 78.9 \times 10^{-12} T_{i,j}^2 \frac{\partial}{\partial \rho_{i,j}} \frac{\partial T_{i,j}}{\partial t} \right) \quad (S42)$$

$$\frac{\partial}{\partial c_{p,i,j}} \frac{\partial k_{i,j}}{\partial t} = \left( \frac{-2.37 \times 10^{-4} \frac{\partial}{\partial c_{p,i,j}} \frac{\partial T_{i,j}}{\partial t}}{(0.037 + 2.37 \times 10^{-4} T_{i,j})^2} + 3 \times 78.9 \times 10^{-12} T_{i,j}^2 \frac{\partial}{\partial c_{p,i,j}} \frac{\partial T_{i,j}}{\partial t} \right) \quad (S43)$$

The same process is repeated for all temperatures and properties ( $k$ ,  $\rho$ , and  $c_p$ ) at every node within the system excluding the coolant in order to obtain all Jacobian terms.

## References

1. Holdampf, S.A.; Osborne, A.G.; Deinert, M.R. Validation of Coolant Thermal Response in a Transient Finite Difference Thermal Transport Model with Applications to Fast Spectrum Reactors. *EPJ Web Conf.* **2021**, *247*, 07018, doi:10.1051/epjconf/202124707018.
2. Waltar, A.E.; Todd, D.R.; Tsvetkov, P.V. *Fast Spectrum Reactors*; 3rd ed.; Springer: New York, 2012; ISBN 978-1-4419-9571-1.
3. Nellis; Klein *Heat Transfer*; Cambridge University Press, 2012; ISBN 978-1-107-67137-9.
4. *Thermophysical Properties of Materials for Nuclear Engineering: A Tutorial and Collection of Data*; International Atomic Energy Agency: Vienna, 2008;
5. Lamarsh, J.; Baratta, A. *Introduction to Nuclear Engineering*; 3rd ed.; Prentice Hall: New Jersey, 2001; ISBN 0-201-82498-1.
6. Luscher, W.G.; Geelhood, K.J. *Material Property Correlations: Comparisons between FRAPCON-3.4, FRAPTRAN 1.4, and MATPRO*; United States Nuclear Regulatory Commission, 2011;
7. *Matlab*; The MathWorks: Natick, Massachusetts, USA;
8. Flores y Flores, A.; Matuzas, V.; Perez-Martin, S.; Bandini, G.; Ederli, S.; Ammirabile, L.; Pfrang, W. Analysis of ASTEC-Na Capabilities for Simulating a Loss of Flow CABRI Experiment. *Ann. Nucl. Energy* **2016**, *94*, 175–188, doi:10.1016/j.anucene.2016.02.032.
9. Rasband, W.S. *ImageJ*; U.S. National Institutes of Health: Bethesda, Maryland, USA, 1997;
10. Hessman, F.V. *Figure Calibration ImageJ Plugin*; Institut für Astrophysik, University of Göttingen: Göttingen, Germany, 2009;
11. Girault, N.; IRSN Centre de Cadarache, Astec-Na CABRI BI1 Benchmark 2019.
12. Dunn, F.E. *The SAS4A/SASSYS-1 Safety Analysis Code System Chapter 3: Steady-State and Transient Thermal Hydraulics in Core Assemblies*; Argonne National Laboratory: Lemont, Illinois, 2017;
13. Argonne National Laboratories Software: SAS4a/SASSYS-1 (Reactor Dynamics and Safety Analysis Code. *Nucl. Eng. Div.*
14. Bandini, G.; Ederli, S.; Perez-Martin, S.; Haselbauer, M.; Pfrang, W.; Herranz, L.E.; Berna, C.; Matuzas, V.; Flores y Flores, A.; Girault, N.; et al. ASTEC-Na Code: Thermal-Hydraulic Model Validation and Benchmarking with Other Codes. *Ann. Nucl. Energy* **2018**, *119*, 427–439, doi:10.1016/j.anucene.2017.12.016.
15. Perez-Martin, S.; Pfrang, W.; Haselbauer, M. Analysis of the CABRI-1 Single Fuel Pin LOF Experiment BI1 with SAS-SFR Code Including Two-Phase Sodium

- Behaviour. In Proceedings of the Proceedings of ICAPP 2014; Charlotte, NC, USA, April 6 2014.
16. Philipponneau, Y. Thermal Conductivity of (U, Pu)O<sub>2-x</sub> Mixed Oxide Fuel. *J. Nucl. Mater.* **1992**, 188, 194–197, doi:10.1016/0022-3115(92)90470-6.
  17. *Status and Trends of Nuclear Fuels Technology for Sodium Cooled Fast Reactors*; IAEA Nuclear Energy Series; IAEA: Vienna, Austria, 2011;
  18. Fink, J.K.; Leibowitz, L. *Thermodynamic and Transport Properties of Sodium Liquid and Vapor*; 1995; p. ANL/RE--95/2, 94649;
  19. Lassmann, K.; Hohlefeld, F. The Revised URGAP Model to Describe the Gap Conductance between Fuel and Cladding. *Nucl. Eng. Des.* **1987**, 103, 215–221, doi:10.1016/0029-5493(87)90275-5.
  20. Lassmann, K. URGAP: A Gap Conductance Model for Transient Conditions.; Preston, United Kingdom, 1982.
  21. Peterson, H. *The Properties of Helium: Density, Specific Heats, Viscosity, and Thermal Conductivity at Pressures from 1 to 100 Bar and from Room Temperature to about 1800 K*; Riso Report; Danish Atomic Energy Commission: Denmark, 1970;
  22. Fink, J.K. Thermophysical Properties of Uranium Dioxide. *J. Nucl. Mater.* **2000**, 279, 1–18, doi:10.1016/S0022-3115(99)00273-1.